

# Focal Depth Estimation: A Calibration-Free, Subject- and Daytime Invariant Approach

Benedikt W. Hosp, Björn Severitt, Rajat Agarwala ZEISS Vision Science Lab, University of Tübingen  
Evgenia Rusak Robust Machine Learning, University of Tübingen  
Yannick Sauer, Siegfried Wahl ZEISS Vision Care GmbH

**Abstract**—In an era where personalized technology is increasingly intertwined with daily life, traditional eye-tracking systems and autofocus glasses face a significant challenge: the need for frequent, user-specific calibration, which impedes their practicality. This study introduces a groundbreaking calibration-free method for estimating focal depth, leveraging machine learning techniques to analyze eye movement features within short sequences. Our approach, distinguished by its innovative use of LSTM networks and domain-specific feature engineering, achieves a mean absolute error (MAE) of less than 10 cm, setting a new focal depth estimation accuracy standard. This advancement promises to enhance the usability of autofocus glasses and pave the way for their seamless integration into extended reality environments, marking a significant leap forward in personalized visual technology.

**Index Terms**—vision, focus, depth estimation, vergence, eye-tracking, machine learning, calibration-free

## I. INTRODUCTION

IN recent years, the landscape of Virtual Reality (VR) has undergone transformative changes, significantly influencing various sectors by enhancing accessibility and expanding its market presence. Alongside VR's growth, smart glasses technology has advanced, with VR serving as a crucial testing ground for innovative algorithms [15]. A notable area of innovation within smart glasses technology is the development of autofocus glasses, designed to address presbyopia - a condition that diminishes the eye's ability to focus on close objects as people age, affecting billions worldwide [3, 8]. Traditional correction methods, such as bifocal or multifocal lenses, often fall short of mimicking the eye's natural focusing capability, leading to restricted gaze and visual inconvenience [31, 19]. Progressive lenses may offer some correction but may introduce aberrations in the periphery [9, 43]. Autofocus glasses, leveraging optical-quality liquids in flexible membranes to dynamically adjust focal length, represent a more natural and innovative solution for presbyopia [5]. Despite their potential, existing autofocus solutions face limitations due to manual focus adjustments and a limited focus range [46], impacting user comfort and adaptability. Furthermore, the autofocus field shows many evaluation metrics but lacks detailed algorithm explanations, limiting understanding and hindering advancements [1, 55]. A significant barrier to the widespread adoption of autofocus

is the cumbersome need for frequent user-specific calibration, significantly limiting the technology's practicality [38]. Previous efforts in focus depth estimation have made strides but often rely on extensive calibration, lack generalizability, and demand significant computational resources [56]. This introduces a substantial obstacle to the seamless integration of autofocus glasses into daily life, highlighting the need for a novel approach to overcome these limitations [21, 40].

In this context, machine learning (ML) emerges as a beacon of innovation, promising to transcend the traditional calibration constraints. This paper introduces the Foveal Attention Long Short-Term Memory Network (FOVAL). This novel spatiotemporal sequential model achieves a calibration-free and daytime invariant focal depth estimation by analyzing eye vergence angle data [27, 39] and intense feature engineering based on domain knowledge. FOVAL marks a significant advance by providing a robust, user-friendly solution that adapts to diverse environmental conditions without the need for frequent recalibration, showcasing the potential of ML to revolutionize personalized technology. FOVAL is distinguished by its technical innovations, including using Long Short-Term Memory (LSTM) layers [14], feature engineering, and advanced preprocessing techniques. Combining these elements enables the model to generalize effectively to new subjects without prior calibration. The optimization of model architecture - incorporating LSTM, normalization layers, and max pooling - underpins the model's exceptional performance, demonstrating the profound impact of ML in overcoming traditional challenges in personalized technology. FOVAL's elimination of the need for calibration dramatically enhances the usability of autofocus glasses, making advanced vision correction more accessible and convenient for users. This technology has the potential to significantly elevate visual acuity and quality of life for those affected by presbyopia, setting a new standard for user-friendly technology integration.

The applications of depth estimation extend well beyond the realm of autofocus glasses, touching on fields as diverse as microscopy [17], VR, and augmented reality (AR) [24]. Specifically, in medical areas like microscopy, arthroscopy, and robotic surgery, precise depth estimation can revolutionize how we visualize and analyze microscopic entities, enhancing the clarity and depth of 3D imaging to understand cellular structures and interactions better [44, 30, 17]. This is especially present in microscopic surgery, where optimal

depth adjustment of the camera during surgery can be handled with such a model as FOVAL [4, 28]. Optimized human focus-based depth estimation can improve medical surgery and diagnostics. In VR and AR, depth estimation is pivotal in creating immersive and interactive experiences by reducing data size while retaining high resolution on focused depth planes [51] and improving perceptual realism [24]. VR enables rendering environments with realistic spatial dynamics, improving user immersion and interaction within virtual spaces [48]. For AR, accurate depth estimation allows for the seamless integration of digital objects into the real world [50, 34], showing accurate 3D images [49] enhancing applications in education, design, and entertainment [22] but also in human-vehicle interaction for autonomous driving [48]. The ability to accurately estimate depth in real-time can significantly improve AR glasses' performance and user experience, making them more practical for various applications, from industrial design to augmented learning environments.

This paper introduces FOVAL - a novel calibration-free method for estimating focal depth, which leverages LSTM networks and domain-specific feature engineering. Our method significantly improves the accuracy and usability of autofocus glasses, achieving a mean absolute error (MAE) of less than 10 cm, and outperforms all state-of-the-art methods in focal depth estimation. Furthermore, by eliminating the need for user-specific calibration, we enhance the practicality of these devices for daily use. In the following section II, we describe details about the methods we use, including data collection, the data preprocessing pipeline, and model development; Section IV presents the results of our evaluation of the model, demonstrating the efficacy of our approach through comparative analysis; and Section V we recapitulate our findings and discusses the implications, limitations, and potential future applications of our findings.

## II. METHODS

For the development and evaluation of our model, we collected data from 25 emmetropic individuals, meaning they had no need for corrective lenses and possessed normal vision (good vision). Of these participants, 11 identified as male and 14 as female, with an average age of 31.68 years (standard deviation = 11.71). Two additional participants were excluded due to issues with eye convergence. All remaining participants were free from any known eye diseases. The study followed ethical guidelines and received approval from the Faculty of Medicine Ethics Committee of the University of Tübingen under reference number 439/2020BO. All subjects gave consent for their data. We collected the dataset in a VR scene showing a sphere with a fixation cross traveling back and forth from 0.35 to 3 meters in a spiral movement on an XTAL VR Headset [54]. Eye vectors and origins (both in headset coordinates) have been recorded and serve as input features to the model. The complete dataset consists of 282080 samples of all individuals combined. The following paragraphs outline the workflow for creating the model. This section is divided

into several parts, following general best practices for building a machine-learning model. Particular emphasis is given to the loss function and the feature engineering part based on domain knowledge (detailed mathematical notations are added to the appendix IX, which most influences model performance). The data cleaning steps contain data preprocessing necessary to increase the model's robustness against errors in sensor input and outliers. After preprocessing, we describe the dataset splitting and feature space, which is essential when working with human gaze data, followed by the data normalization and transformation steps. Finally, we describe the model architecture.

### A. Data Preprocessing Pipeline

The data preprocessing pipeline involves several key steps to ensure the data is prepared effectively for the machine learning model. Here, we outline the steps in the order they are applied:

#### Step 1: Data Cleaning

Anomalies and outliers were identified and eliminated through a detailed removal process. We employed a rolling mean window (window size = 5, threshold = 10) for the target variable to detect context-specific, short-term anomalies that can occur due to input signal noise. Window size and threshold have been defined empirically. This approach captures transient deviations from the mean over time. For the features, we utilized the Interquartile Range (IQR) method [53] over the time dimension to enhance data consistency. The IQR method is better suited to identify statistically rare events within the whole range of the features, capturing both short-term and long-term outliers. The window calculation process is formalized in Equations 1, 2, and 3.  $GT_{depth_i}$  represents the ground truth depth value at the  $i$ -th position in the dataset,  $W_i$  represent the window of values around  $GT_{depth_i}$ , defined by a specified window size. For each  $GT_{depth_i}$  in the dataset, we define a window  $W_i$  of values centered around  $i$ , with size  $window_{size}$ . The window is defined as:

$$W_i = \{GT_{depth_{start}}, \dots, GT_{depth_{end}}\} \quad (1)$$

where

$$start = \max\left(i - \frac{window_{size}}{2}, 0\right) \quad (2)$$

$$end = \min\left(i + \frac{window_{size}}{2} + 1, N\right) \quad (3)$$

and  $N$  is the total number of observations in the dataset of one subject.  $mean(W_i)$  represents the mean value of the ground truth depths within the window  $W_i$ , and  $threshold$  represents the predefined threshold for outlier detection. The window's mean is then calculated with Equation 4. A value  $GT_{depth_i}$  is considered an outlier if the absolute difference between  $GT_{depth_i}$  and the mean of  $W_i$  exceeds the threshold (Equation 5).

$$mean(W_i) = \frac{1}{|W_i|} \sum_{j=start}^{end} GT_{depth_j} \quad (4)$$

$$\text{Outlier if } |GT_{depth_i} - \text{mean}(W_i)| > \text{threshold} \quad (5)$$

For *removing data outliers* within our feature space, we utilize the IQR method [53]. This technique involves computing the first ( $Q1$ ) and third ( $Q3$ ) quartiles for each column within our dataset, with the IQR defined as the difference between these quartiles, as illustrated in Equation 6. Subsequently, outliers within each feature column are identified and eliminated based on the criteria outlined in Equation 7, where  $df$  symbolizes our data frame. This operation is executed independently for each column to ensure the nuanced characteristics of each feature are adequately considered.

$$IQR = Q3 - Q1 \quad (6)$$

$$Q3 + 1.5 \times IQR < df_{\text{column}} < Q1 - 1.5 \times IQR \quad (7)$$

Here,  $df$  refers to our data frame, which encapsulates the entirety of the data of one subject. For each feature column in  $df$ , denoted as  $df_{\text{column}}$ , we calculate  $Q1$ ,  $Q3$ , and  $IQR$  to establish the bounds for identifying outliers. The 'mask' generated by Equation 7 is a boolean array specific to each column, indicating which values fall outside the accepted range (defined by 1.5 times the IQR below  $Q1$  and above  $Q3$ ), thereby flagging them as outliers. This approach ensures that outlier detection and removal are tailored to the distribution of each feature, maintaining the integrity of our dataset by selectively filtering outliers based on the statistical properties of individual columns. Rows in the dataset are considered outliers if they fall outside the range specified by this mask and are removed. Outliers can significantly skew statistical measures such as the mean, variance, and standard deviation, resulting in unreliable data representation. Removing outliers provides a more accurate depiction of the data distribution, enhancing the reliability of these measures. While anomalies are detected within small, moving windows, affecting only a localized subset of data points at a time, outliers are detected across the entire dataset, affecting global statistical measures. Therefore, anomalies have a limited impact because they are transient and localized. In contrast, outliers can drastically shift the overall mean due to their extreme values relative to the rest of the data. Many machine learning models assume that the data follows a particular distribution, and outliers can violate these assumptions, leading to poor model performance. Therefore, outlier removal often improves model accuracy and generalization [42, 52, 33, 29]. Outliers can also introduce noise into the dataset, which confuses the model during Training. By removing outliers, we reduce this noise, enabling the model to focus on the underlying patterns in the data. Additionally, outliers can stem from data entry errors

or anomalies in data collection. Identifying and removing these outliers prevents such errors from negatively impacting the analysis and conclusions. Removing outliers ensures that statistical test results are more robust and reflective of the actual data characteristics. This is particularly crucial during data transformation, where outliers can significantly impact the choice of transformation.

### Step 2: Data Balancing

As soon as the data for each subject is cleaned, we continue with data balancing. To do so, we combine over- and undersampling (Equation 10) before binning the target variable. This process involved quantizing the target variable into a predetermined number of bins, ensuring an equal distribution of samples across each bin. Since the dataset's data is mainly spread across 0 to 600 cm, we defined bins of 10 cm to ensure a balanced amount of samples for at least each 10 cm bin, resulting in 60 bins. We chose the bin size based on the visualization of the dataset as a trade-off between covering a wide range of possible values and having a substantive amount of representative samples for each bin. This strategy ensures that the model is not biased towards more frequently occurring data ranges. In the first step, we divide the target variable,  $GT_{depth_i}$ , into a predetermined number of bins ( $N_{bins}$ ), where  $\text{Bin}(\cdot)$  denotes the binning operation, and  $N_{bins} = 60$  in this context (Equation 8). Next, we calculate the mean count per bin  $\bar{C}$ , where  $C_i$  is the count of samples in the  $i$ -th bin (Equation 9). To ensure that each bin has a sample count close to the mean count  $\bar{C}$ , we perform resampling. For bin  $i$ , the resampled bin data,  $D'_i$ , is obtained using Equation 10, where  $|D_i|$  is the count of samples in bin  $i$ , and  $\text{Resample}(\cdot)$  denotes the resampling operation. This process involves random oversampling or undersampling of each bin to match the mean count  $\bar{C}$ . Finally, the resampled bin data from all bins are concatenated to form a balanced dataset as described in Equation 11.

To ensure that each bin has a sample count close to the mean count  $\bar{C}$ , we apply the following resampling strategy: If the number of samples in a bin  $|D_i|$  is less than the mean count  $\bar{C}$ , we perform oversampling with replacement to increase the sample count to  $\lceil \bar{C} \rceil$ . If the number of samples in a bin  $|D_i|$  is greater than the mean count  $\bar{C}$ , we perform undersampling without replacement to reduce the sample count to  $\lceil \bar{C} \rceil$ . And if the number of samples in a bin  $|D_i|$  is equal to the mean count  $\bar{C}$ , no resampling is necessary. The following equation represents this process:

$$GT_{depth_{bin}} = \text{Bin}(GT_{depth}, N_{bins}) \quad (8)$$

$$\bar{C} = \frac{1}{N_{bins}} \sum_{i=1}^{N_{bins}} C_i \quad (9)$$

$$D'_i = \begin{cases} \text{Resample}(D_i, \text{replace} = \text{True}, n = \lceil \bar{C} \rceil), & \text{if } |D_i| < \bar{C} \\ \text{Resample}(D_i, \text{replace} = \text{False}, n = \lceil \bar{C} \rceil), & \text{if } |D_i| > \bar{C} \\ D_i, & \text{otherwise} \end{cases} \quad (10)$$

$$\text{Balanced dataset} = \bigcup_{i=1}^{N_{bins}} D'_i \quad (11)$$

This binning and resampling process is crucial for addressing imbalances in the distribution of the target variable across the dataset. By ensuring each bin has a similar number of samples, we enhance the generalizability of the machine learning model. This balanced approach reduces bias towards over-represented values, making predictions more accurate and fair. Additionally, it improves the model’s performance across the range of the target variable by ensuring adequate representation of each data segment, leading to more reliable and consistent results.

### Step 3: Splitting

To incorporate the intricate risks of biophysical data, we also ensured the generalizability of our machine-learning model by employing a systematic approach to data splitting using the K-Fold cross-validation (K-Fold CV) technique in a subject-wise manner. This method is pivotal for assessing the model’s performance and ability to generalize to unseen data. We initialized the KFold cross-validator from the Scikit-Learn library [41] with a predetermined number of splits,  $n\_splits = \text{number of subjects}$ , and set shuffle to True to randomize the data before splitting it. This effectively is a Leave-One-Out Cross-Validation (LOOCV) approach as a particular case of KFold CV. The randomization is crucial for mitigating any potential bias stemming from the original ordering of the data. To ensure the reproducibility of our results, we fixed the random state parameter to 42.

$$KFold(splits = n\_splits, shuffle = True, random state = 42) \quad (12)$$

To maintain the integrity of subject data and avoid data leakage, we performed the splits based on unique subjects in the dataset (subject-wise splitting, see [16] for more details). This approach ensures that all data from a single subject is exclusively in the Training, validation, or testing set, which is critical for evaluating the model’s performance in real-world scenarios. We created splits for training and validation, again ensuring there was no overlap of subjects between these sets. Inference is then done on unseen subjects. This meticulous data splitting and validation approach is foundational for developing accurate and reliable machine learning models. By ensuring that our model is tested on unseen data in a manner that mimics real-world application scenarios, we can confidently assess its generalizability and readiness for deployment. Moreover, subject-based splitting guards against overfitting and ensures that our model’s performance metrics indicate its true predictive power.

### Step 4: Feature space

Based on the input sequences of 10 temporally consecutive samples of 12 input features (eye vector left and right (x,y,z) and eye origin, we enhanced the model’s predictive power by

deriving new features from the 12 input features and one target variable (GT depth).

The features are derived from the optical axis, which is defined as the line that passes through the centers of the eye’s optical components, such as the cornea, the pupil, and the lens, and is perpendicular to these surfaces. In contrast, the visual axis is defined by a line that is not perpendicular to the retina but instead ends on the fovea of the eye. Typically, eye-tracking methods need to estimate this offset to estimate the precise point of regard (POR) in 3D space because only the optical axis is easily detectable from eye images directly. However, as we do not rely on the actual POG but instead on relative movements, we do not need to know the visual axis and can use uncalibrated eye images as input.

Our features can be divided into primary, ratios & differences, and higher-order dynamics of eye movements. In the following section, we give an overview of the features and their meaning. For the particular implementations, please see Appendix IX for an exhaustive list of equations.

a) *Eye Vergence Angle*: The Eye Vergence Angle (EVA) is pivotal in understanding how the eyes adjust their lines of sight when focusing on an object. This angle results from both eyes’ simultaneous inward or outward movement to maintain single binocular vision as they shift focus across objects at varying distances. EVA provides critical insights into the focal depth and the mechanisms underlying 3D perception. It is essential for grasping the spatial dynamics of visual perception. We normalized the angle between different subjects to compare it. Additionally, the conversion of EVA to a cosine metric simplifies some analyses. A key derivative of EVA, vergence depth, offers a quantifiable measure of the focal depth but provides the most reliable estimates only within a specific mid-range due to the nonlinear relationship between EVA and depth.

b) *Eye Direction Vectors*: Beyond the EVA, we analyze changes in eye direction vectors (EDV) to illuminate eye alignment and focus disparities. This includes assessing differences in vector components between the eyes and calculating the Euclidean distance between focus points (intersections of the vectors) to determine the convergence or divergence in gaze. The directional magnitudes for each eye’s gaze direction are compared to reveal potential asymmetries in eye movement strength. While the intersection of EDVs on the z-axis can be informative about the focused depth, even slight inherent noise and errors in the estimation of the EDVs can introduce high variation in depth estimation. This is one major problem that causes eye-tracking for depth perception to be not as reliable as needed.

c) *Ratios and Differences*: Another group of features can be described as ratios and differences. Here, we explore the ratio of directional magnitudes by dividing one eye’s directional magnitude by the other’s, shedding light on eye movements and gaze focus asymmetries. Additionally, analyzing the magnitudes of individual dimensions uncovers insights into the relative orientations and dominance in gaze direction. The feature examining horizontal to vertical disparities in gaze may reveal preferred axes of movement or alignment. Key to our analysis is the quantification of eye movement rates—velocity

and acceleration—highlighting the agility and speed at which eyes move. This is essential for identifying rapid attention shifts or differentiating between types of eye movements, such as saccades and smooth pursuits [36]. The relative change in EVA captures temporal shifts in depth perception, examining how focus adapts to changing stimuli. We also delve into the angular differences between the eyes' gaze directions, a critical factor in diagnosing binocular coordination issues. The ratios of directional magnitudes and world gaze direction components enable a normalized comparison of eye movement strengths and orientations, enriching data analysis by accounting for individual eye movement characteristics. Lastly, metrics concerning gaze point distance and depth difference are included, providing valuable perspectives on the visual system's spatial positioning and depth perception capabilities, essential for 3D visualization and AR applications.

#### Step 5: Normalization

The next step in the preprocessing pipeline is to normalize the features. Normalization is applied in two steps to the datasets, which is particularly useful in scenarios where data comes from multiple subjects, each potentially with different baselines or scales of measurement.

Given a dataset  $D$  with multiple subjects, the two-step normalization process involves applying global normalization to  $D$  (see equation 13), obtaining  $D_{\text{global\_norm}}$ , and then for each subject in  $D_{\text{global\_norm}}$ , applying subject-wise normalization to obtain the final normalized dataset  $D_{\text{final\_norm}}$  (see equation 14). The normalization per subject is to account for individual variations, ensuring the model learns generalized patterns rather than subject-specific characteristics.

*Step 5.1: Global Normalization:* The global normalization process applies a *Robust Scaler* [13] to the dataset's features, excluding specific columns such as GT Depth. This scaling technique is particularly effective in datasets with outliers, as it uses the interquartile range for scaling, thereby reducing the influence of extreme values such as outliers. Given a feature vector  $X = [x_1, x_2, \dots, x_n]$ , the *Robust Scaler* transforms  $X$  into  $X'$  by computing:

$$X' = \frac{X - \text{Median}(X)}{\text{IQR}(X)} \quad (13)$$

where  $\text{Median}(X)$  is the median of the feature values in  $X$ ,  $\text{IQR}(X)$  is the Interquartile Range of  $X$ , calculated as  $\text{IQR}(X) = Q3(X) - Q1(X)$ , with  $Q3(X)$  and  $Q1(X)$  representing the third and first quartiles of  $X$ , respectively. The transformed dataset  $D'$  then contains the normalized features. We use a scaler that is robust to outliers to ensure stability and robustness in our preprocessing pipeline, accounting for any residual outliers, future data variations, and skewed distributions.

For global normalization, the statistics (median and IQR) are calculated using the training set. These statistics are then applied to normalize the test set, ensuring that the normalization process is consistent and does not introduce data leakage. Even after removing outliers, global normalization

remains essential because it ensures that the overall scale of the data is consistent, making the dataset more robust to variations. The global normalization step adjusts the data on a broader scale, ensuring that features from different subjects and conditions are comparable. This step is crucial to avoid biases in the model training process caused by different feature scales.

*Step 5.2: Subjective (Subject-Wise) Normalization:* Data is further normalized on a per-subject basis after global normalization. This step accounts for individual differences, ensuring that the model does not learn from these variations but from the underlying patterns.

For a subject  $s$  with data  $X'_s$ , subject-wise normalization is applied as:

$$X'_{s,\text{normalized}} = \frac{X'_s - \text{Median}(X'_s)}{\text{IQR}(X'_s)} \quad (14)$$

Subject-wise normalization is calculated and applied directly to each subject's data, ensuring that intra-subject variability is appropriately handled. By combining these two normalization steps, we ensure that our model is trained on data that is both globally and individually normalized, enhancing its generalizability. This process is repeated for each unique subject in the dataset, ensuring individual data scales are aligned. Especially in physiological or behavioral data, measurements can significantly differ between subjects due to innate individual differences. Subjective normalization is critical to handling inter-subject variability. It further improves model generalization by ensuring the model learns from normalized features, allowing it to better generalize across subjects not part of the training data. Another important aspect is a fair comparison. It ensures that features from different subjects are on a comparable scale, making statistical analysis and machine learning modeling more effective and fair.

#### Step 6: Feature Transformation

Feature transformations ensure that each feature in the dataset is transformed to achieve a more normal distribution, supporting the assumptions of many machine learning algorithms and improving overall model performance [7, 37, 20]. Different mathematical transformations are tested on the training dataset for each feature to achieve a distribution closer to normal distribution characteristics, which can improve the performance of specific machine-learning models. While normalization typically scales the data to a standard range or distribution, it does not necessarily transform the data to follow a Gaussian distribution. Therefore, applying transformations such as logarithmic, square root, or Box-Cox is necessary to address skewness and other distributional issues that normalization alone cannot resolve.

The ideal transformation minimizes the distance to the normal distribution characteristics defined by skewness and kurtosis. Skewness measures the asymmetry of the data distribution, with an ideal skewness of 0 indicating a perfectly symmetrical distribution. Kurtosis measures the tailedness of the distribution, with an ideal kurtosis of 3 indicating a normal

distribution. Transforming the data to be more Gaussian-like (normal distribution) can support faster convergence in machine learning models and improve their performance and accuracy [20, 37]. This step accounts for generalizability and robustness, too.

Machine learning algorithms often assume that input data follows a normal distribution. Skewed data or data with extreme kurtosis can lead to biases in model training and prediction errors. Addressing these issues helps create more robust models. For specific statistical models (like linear regression), meeting normality assumptions leads to more reliable and interpretable estimates [20, 37]. Transforming features to have similar distributions also makes them more comparable and more accessible to visualize, facilitating better understanding and interpretation.

To determine the best transformation, we apply the following steps:

- 1) **Calculate Original Skewness and Kurtosis:** For each feature in the dataset, calculate the original skewness and kurtosis.
- 2) **Apply Transformations:** Apply predefined transformation techniques (e.g., log transformation, square root transformation, Box-Cox transformation) to each feature.
- 3) **Evaluate Transformations:** Calculate the resulting skewness and kurtosis for each transformed feature for each transformation.
- 4) **Compute Distance Metric:** Compute a distance metric for each transformation, measuring how far the transformed data's skewness and kurtosis are from the ideal values (skewness = 0, kurtosis = 3).
- 5) **Select Best Transformation:** The transformation that minimizes the distance metric is considered the best for that feature.
- 6) **Save Best Transformation:** Save the best transformation for each feature to apply the same transformation to the validation dataset.

The approach of transforming features to achieve a normal distribution is well-documented in the literature. Box and Cox's transformation [7] is a commonly used method to stabilize variance and make the data more normally distributed. Similarly, Osborne [37] discusses improving data transformations for statistical analysis. These transformations are standard procedures in data preprocessing aimed at enhancing the robustness and accuracy of machine learning models.

#### Step 7: Scaling Target

To improve the performance and stability of our machine learning models, we rescale the target variable to align with the input features. However, the reasons for rescaling the target variable are multi-fold:

Rescaling ensures that the model's output values are within a comparable range to the input features, facilitating faster convergence during Training. Significant discrepancies between the scales of input features and target values can lead to inefficient optimization processes and slow convergence rates [11]. Working with a wide range of target values can

introduce numerical instabilities, particularly in gradient-based optimization methods. By rescaling the target values to a smaller, more manageable range, we mitigate these instabilities and promote a more stable training process [25]. Maintaining consistency in the scaling of input features and target variables helps the model learn the relationships between inputs and outputs more effectively. This consistency can result in more accurate predictions and better generalization to unseen data [6]. Rescaling target variables is a standard practice in machine learning, especially in regression tasks. It ensures that the model's loss function operates within a consistent scale, which is crucial for effective training [12]. To ensure that the model's predictions are interpretable in the context of the original data, the scaler used during the training process must be saved. This saved scaler is then used to apply an inverse transformation to the model's predictions.

During the training process, the target variable  $y$  is scaled to improve model performance and Training stability. However, once the model generates predictions, these predictions are in the scaled form. To interpret these predictions correctly, we need to convert them back to the original scale of the target variable. After obtaining the model's predictions  $\hat{y}$  on the test set or new data, we apply the inverse transformation to convert them back to the original scale. This process involves using the saved scaler to reverse the scaling operation applied during Training.

The target variable is initially measured in centimeters, with values ranging from 0 to around 900 cm, corresponding to a depth perception range from 0.0 to 9 meters based on the typical eye vergence range. To standardize this range and make it more manageable for computational purposes, the target variable is scaled to a range of 0 to 1000 cm using a MinMax Scaler transformation. This transformation adjusts the values of the target variable to the specified range [0, 1000].

The transformation for a value  $y$  in the original dataset to the scaled value  $y'$  is given by:

$$y' = a + \frac{(y - y_{\min}) \times (b - a)}{y_{\max} - y_{\min}}$$

where  $y_{\min}$  and  $y_{\max}$  are the minimum and maximum values of the target variable in the training dataset, respectively, and  $a$  and  $b$  are the bounds of the new scaling range, with  $a = 0$  and  $b = 1000$  in our case.

We chose the 0 to 1000 range to encompass a depth perception range of 0 to 10 meters, considering that eye movements can change depth perception up to approximately 10 meters, beyond which it is considered infinity. This range ensures that the model is prepared for all kinds of data that might be fed into it in the future, including maximum depth perception scenarios.

During development, the MinMax Scaler performed better than typical scaling methods by preserving the relative distances between data points and improving the model's performance. The 0 to 1000 range, while larger than the original scale, ensures that the scaled values are standardized and more suitable for various computational operations and visualizations.

### Step 8: Sequence Creation for Time-Series Analysis

As soon as the data is clean, normalized, transformed, and scaled, we structure samples into sequences to capture temporal dependencies within the eye movement data. This approach ensures that the temporal context is preserved, which is crucial for training models on sequential data where the order and timing of observations are essential. Given a dataset  $D$  organized by subject, the process first divides the dataset into subsets  $D_s$ , each corresponding to a unique subject  $s$ , ensuring that sequences are generated within individual subject data.

We generate sequences for a defined sequence length  $L$  by sliding a window of length  $L$  across each subject's data. This means that the sequences overlap, as each new sequence starts one time step after the previous one. For each position  $n$  within the data for subject  $s$ , a sequence  $S_n$  and its corresponding target  $y_n$  are defined as:

$$S_n = \{X_n, X_{n+1}, \dots, X_{n+L-1}\}$$

$$y_n = y_{n+L}$$

where  $X_n$  represents the feature vector at time step  $n$ , and  $y_{n+L}$  is the target value immediately following the sequence. This overlapping sequence generation ensures that temporal dependencies are effectively captured, providing the model with sufficient context for learning.

## III. MODEL

The model's architecture was defined using PyTorch's dynamic computation graph and intuitive API, which makes it ideal for developing complex neural networks. The model was trained using PyTorch's built-in functions for backpropagation and optimization. NumPy was used to handle data arrays and perform numerical operations, while SciPy provided additional mathematical and statistical functions necessary for preprocessing and evaluation.

The training process involves several key components: The choice of *optimizer* is critical for the model's learning efficiency and convergence. Due to its effectiveness in some pre-runs, we picked AdamW [32] (Adam [23] with weight decay). We found that a smooth L1 loss [10] with  $\beta=0.75$  works best for the loss function. Beta has been defined empirically by a hyperparameter search. The Smooth L1 Loss function minimizes prediction errors while balancing the mean absolute error and mean squared error. It is a robust loss function less sensitive to outliers compared to the L2 Loss and has been shown to prevent exploding gradients [45]. It behaves like the L1 Loss when the absolute value of the argument is high and the L2 Loss when the absolute value is small. The loss function is defined as follows, with a beta parameter ( $\beta$ ) controlling the transition:

$$L_{\text{smooth}}(y, \hat{y}) = \begin{cases} 0.5 \times \frac{(y - \hat{y})^2}{\beta} & \text{if } |y - \hat{y}| < \beta \\ |y - \hat{y}| - 0.5 \times \beta & \text{otherwise} \end{cases} \quad (15)$$

The model is trained on  $n-1$  subjects and validated/tested on the one left-out subject, ensuring a rigorous evaluation of

its generalization capability. We train each fold in  $n = 2000$  epochs with a batch size of 460, a weight decay of 0.0906, a learning rate of 0.033, a dropout rate of 0.245, an embedded dimension of 1435, and a fully connected dimension of 1763. After prediction, the scaling of the target variable is inverted to interpret the model's output in the original scale. Performance metrics are then saved for each fold of the cross-validation process. After all folds, the average performance metrics are calculated and reported, providing a comprehensive overview of the model's effectiveness across the entire dataset. We used the Optuna framework with a Tree-structured Parzen Estimator (TPE) Sampler to find the optimal hyperparameters [2].

### A. Architecture

The proposed model employs an architecture to efficiently process sequential data, pinpointing the most critical timestep for further analysis. The input to the model is a temporal sequence of eye movement data from one subject over a given range. Each sequence contains ten consecutive timesteps, with each timestep consisting of 54 features. Given the dataset's structure, we have approximately 28208 sequences in total, ensuring a comprehensive dataset for Training and evaluating the model's performance. Figure 1 illustrates the model's structure, starting with an input of (1, 10, 54) corresponding to a sample/sequence with ten timesteps of 54 features. The input is fed to an LSTM layer with a substantial hidden size of 1435. This design choice enables the model to capture complex dependencies within the input sequence. Following the LSTM layer, a batch normalization [18] layer stabilizes and accelerates learning by normalizing the activations. Crucially, the architecture incorporates a max pooling [26] layer immediately after batch normalization. This layer acts as an "information bottleneck," selectively emphasizing the most significant timestep in the sequence, shown as the encoding step in Figure 1. By focusing on this key timestep, the model aims to distill the essence of the sequential data, ensuring that subsequent processing is concentrated on the most relevant information. After identifying and isolating the pivotal timestep through max pooling, the model introduces a dropout [47] layer with a probability  $p = 0.245$ . This layer randomly excludes a portion of neurons during Training, reducing overfitting and encouraging the model to learn more robust features. The condensed information from the selected timestep undergoes dimensional expansion through two fully connected (FC) layers. The first FC layer enlarges the feature space to 1763 dimensions, allowing the model to explore a broad spectrum of patterns within the critical timestep. The penultimate layer of the model is an exponential linear unit (ELU), which introduces non-linearity to the output, enabling the model to handle complex relationships between the processed timestep and the target variable. A subsequent FC layer decreases the dimensionality to 440, forcing the model to robustly capture intricate patterns before making predictions. This series of operations—from focusing on the most informative part of the sequence to expanding the feature space—allows the model to effectively distill and analyze the essence of the input data, providing a robust framework for understanding and predicting based on sequential patterns.

## Foveal Attention LSTM

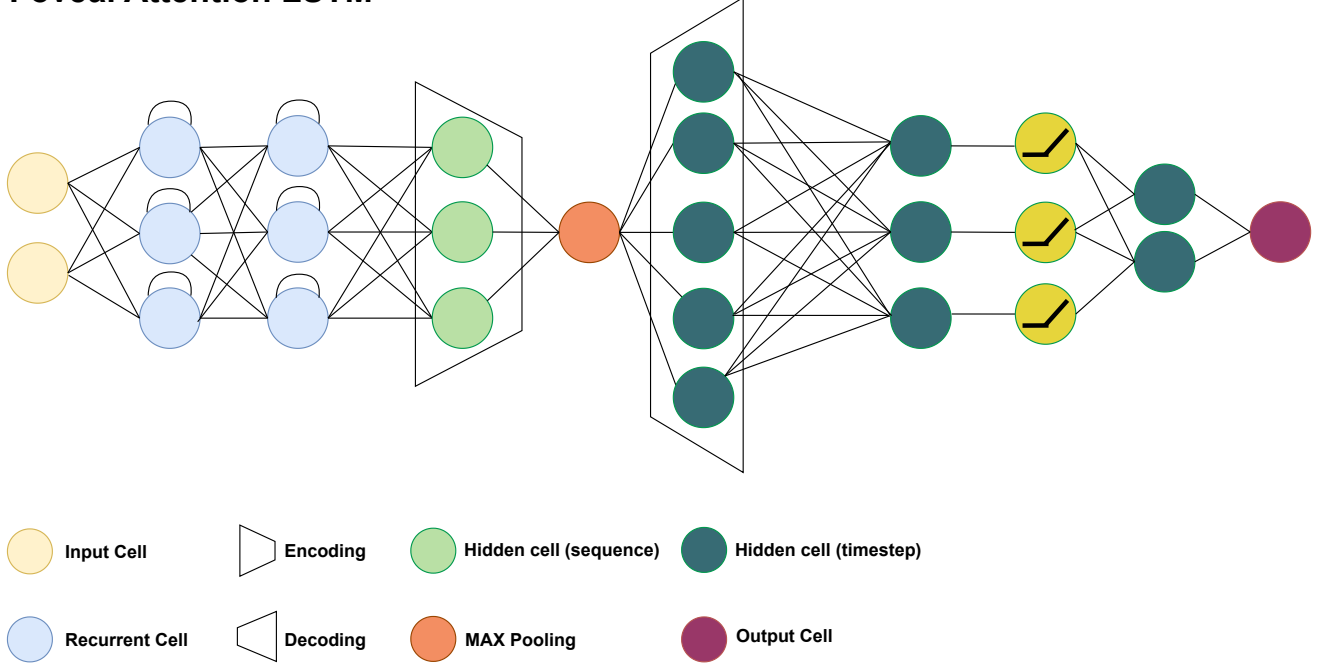


Fig. 1. Schematic representation of the FOVAL processing model. The architecture begins with an LSTM layer (hidden size=1435) to capture temporal dependencies, followed by batch normalization for stabilization. A max-pooling layer then identifies the most critical timestep, acting as an information bottleneck that distills the sequence’s essence. This key timestep is processed through a dropout layer (probability  $p=0.245$ ) to mitigate overfitting. Subsequent fully connected layers progressively expand and shrink the dimensionality (to 1763 and then to 440). This enables the model to explore and identify complex patterns within the critical timestep before the final prediction is made through an exponential linear unit (ELU). This approach emphasizes the extraction and comprehensive analysis of pivotal temporal information.

## IV. EVALUATION

Central to our analysis is a dataset comprising eye movement recordings from 25 emmetropic individuals, which spans a dynamic range of focal depths and includes a diverse age range. This dataset lays a robust foundation for assessing FOVAL’s performance, notably achieving a mean absolute error (MAE) as low as 5.9 cm.

Our comparison between FOVAL, the Mix-TCN model [56], and the geometric vergence (geom. vergence) method was conducted using the reported performance metrics of these models rather than direct computational evaluation. Accessibility constraints primarily drove this decision. Specifically, we did not have access to the dataset used by Zhu [56] for the Mix-TCN model, nor could we utilize their trained model parameters due to their unavailability. Similarly, retraining the Mix-TCN model on our dataset was not feasible without detailed architecture specifics and training protocols. Under these circumstances, the most pragmatic approach was to rely on the performance metrics published by the author, which are assumed to be representative of their models’ capabilities under their respective testing conditions. Although this method does not allow for a controlled, head-to-head comparison under identical data conditions, it still provides a valid frame of reference for evaluating FOVAL’s relative performance and demonstrating its potential advantages in accuracy and usability. In future work, should

the data and models become accessible, a direct comparison would be invaluable for a more detailed and controlled performance analysis.

The performance of FOVAL not only markedly surpasses the Mix-TCN model’s 12.1 cm MAE, reported by Zhu [56], but also outperforms the traditional EVA method (error of 42 to 83 cm [35]), illustrating FOVAL’s adaptability and its transformative potential for autofocal glasses application in everyday life.

In a direct comparison with our dataset, the traditional EVA method reached an MAE of 30 cm. FOVAL, on the other hand, reached a mean MAE of 9.4 cm with a confidence interval between 1.12 and 1.47 cm, starkly contrasting with subject-wise calibrated Mix-TCN’s reported 12.1 cm MAE and traditional EVA. This considerable discrepancy accentuates FOVAL’s superior accuracy and emphasizes the need for future direct comparative analyses to evaluate these models’ efficacy comprehensively.

The FOVAL approach demonstrates a robust performance spectrum, illustrated through its best, average, and worst Mean Absolute Error (MAE) values, the state-of-the-art method from Zhu’s [56], and EVA. As depicted in Figure 2, FOVAL’s performance variability is encoded in a gradient of blues, with its best performance (5.9 cm) outstripping the benchmarked Mix-TCN (12.1 cm) and the traditional EVA method (30.0 cm). The performance of the personal-calibration dependent Mix-TCN model is marked in purple, between FOVAL’s

## Comparison of MAE

MAE of FOVAL (best, average, and worst) and State-of-The-Art methods

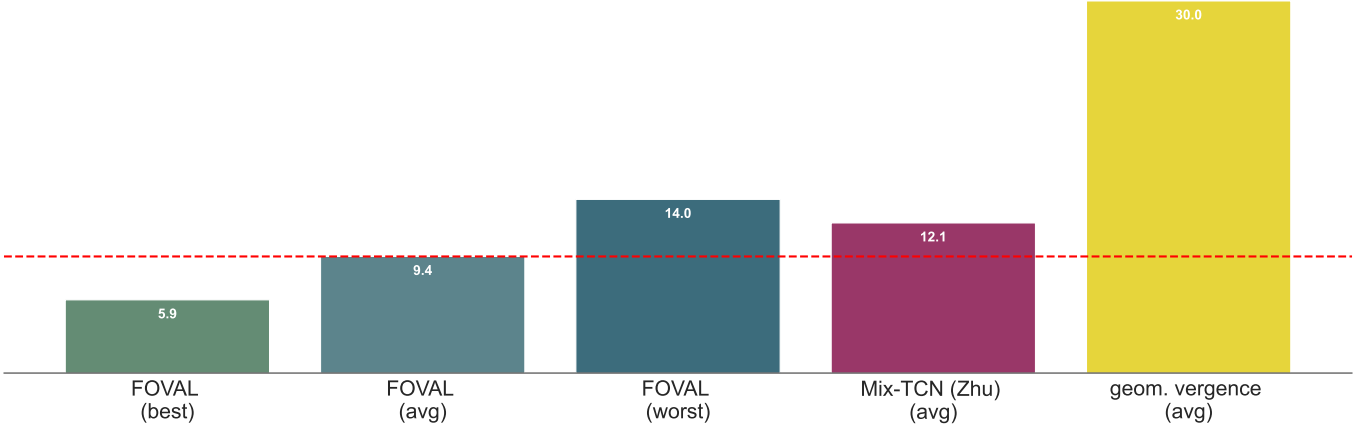


Fig. 2. Direct comparison of FOVAL performance with the current Mix-TCN model by Zhu [56] and the purely geometrically calculated vergence method (geom. vergence). FOVAL achieves a mean absolute error (MAE) as low as 5.9 cm on some subjects, with an average performance of around 9.4 cm, showcasing its superiority over calibration-based state-of-the-art methods like Mix-TCN’s 12.1 cm and the traditional vergence method’s 30 cm. While FOVAL excels in this direct comparison, it is important to note that Zhu’s method was evaluated on a different dataset, and the reported values are based on published metrics.

## Distribution of Residual Errors

Data of all subjects

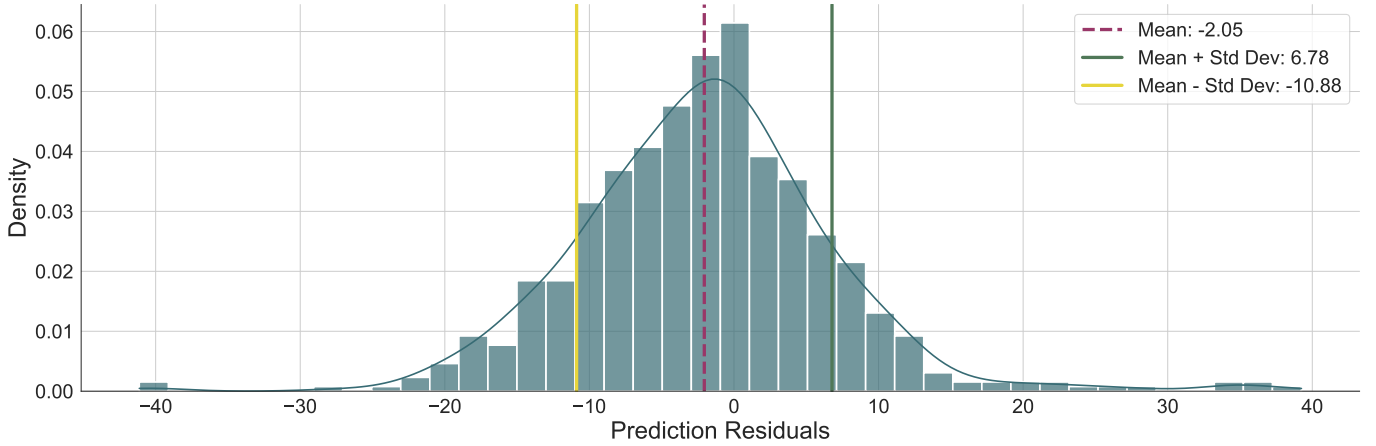


Fig. 3. The histogram of the residuals covering all data from all subjects has its mean at -2.05 cm and standard deviations of -7.64 and 14.62. As such, the distribution is slightly skewed to the right, indicating a tendency to overestimate the focal depth.

average (9.4 cm) and worst outcomes (14.0 cm). At the same time, the EVA method, represented in light yellow, shows the highest MAE.

### A. Distribution of Residual Errors

A closer examination of the prediction errors across the dataset (Figure 3) reveals that the distribution of the residual errors predominantly centers around an MAE of -2.05 cm with a standard deviation of 8.83 cm, indicating a high precision level in focal depth estimation. The histogram is slightly skewed to the right, indicating that FOVAL tends to overestimate the focal depth on average. To better analyze the performance in a more fine-grained way, we analyze the residuals by categorizing them in specific ranges (Figure 4): Less than 1 cm, 1-10 cm, 10-20 cm, and greater than

20 cm. This shows the distribution of residuals in terms of the usability of the system. Residuals smaller than 10 cm are assumed to be small enough for the system to have no negative impact on a real-life application. We see that a majority, around 67.5% of errors, fall within a practically negligible range of under 10 cm, underscoring FOVAL’s real-world applicability [56].

### B. Error Distribution in Binned Ranges

The vergence-angle-to-depth relationship is inherently non-linear, particularly at close and far distances. However, within mid-range distances, this relationship can approximate a more linear trend. This behavior arises because the rate of change in the vergence angle is much more significant at shorter distances, leading to a nonlinear response. As the distance

## Classification of Residuals

Based on measurement accuracy

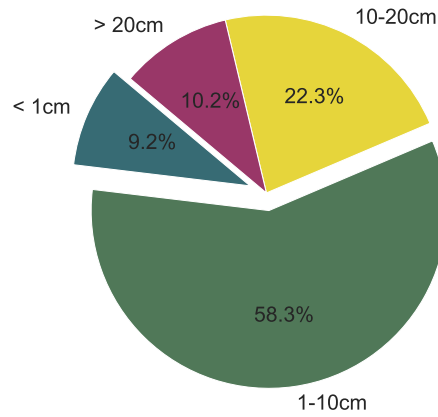


Fig. 4. Categorizing all residuals into performance bins allows for a more detailed interpretation of their distribution. The pie plot reveals that 9.2% of residuals are smaller than 1 cm, 67.5% are smaller than 10 cm, 89.9% are smaller than 20 cm, and only 10.2% of residuals are greater than 20 cm. This indicates that FOVAL can estimate the focal depth with optimal precision for more than 67% of the data and with sufficient precision for approximately 22% of the data. However, 10.2% of the data have residuals indicating insufficient precision in the regression.

## Mean Residuals over Full Range

Mean values of whole dataset with optimal working area

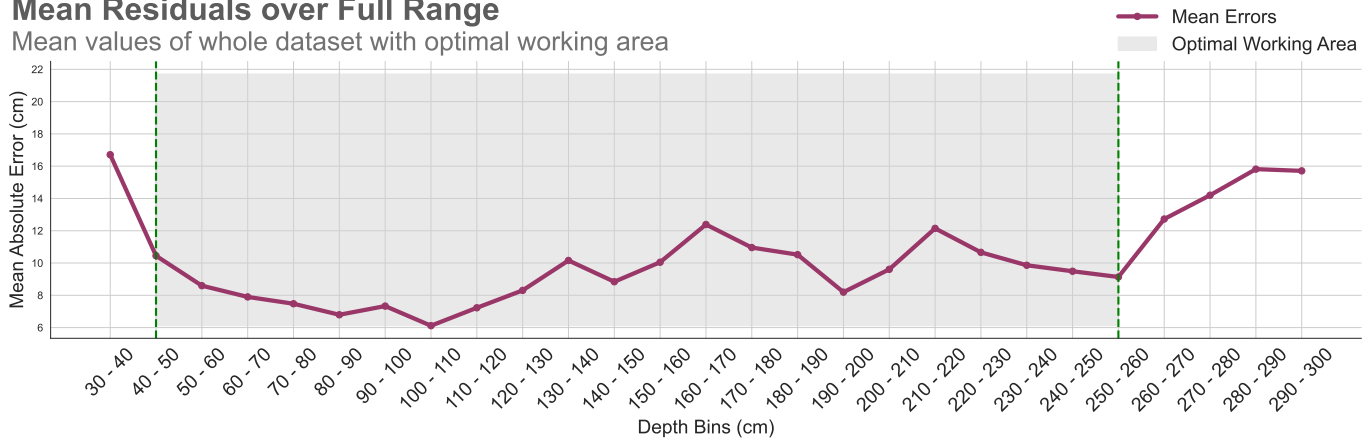


Fig. 5. Separation of average error based on 10 cm depth distance ranges. FOVAL predictions reflect the expected behavior of vergence: nonlinear at short and far distances, with a piecewise linear approximation in mid-distances. The gray area highlights the depth range where FOVAL performs best, indicating optimal prediction accuracy within these mid-range distances. While the curve within the gray area is not perfectly linear, it demonstrates a more stable and predictable pattern compared to the short and far distance ranges.

increases, the rate of change in the vergence angle decreases, which can result in a piecewise linear approximation over certain mid-range distances. At far distances, the vergence angle changes very little, reinforcing the non-linearity of the relationship. Further insights are provided by analyzing the error distribution across different depth bins (Figure 5). The results demonstrate that FOVAL's predictions align closely with the expected behavior of vergence. Specifically, the vergence-to-depth relationship is nonlinear at both close and far distances and piecewise linear in the mid-range. This behavior is reflected in the performance of FOVAL, which shows optimal prediction accuracy within the mid-range distances where the piecewise linear relationship is most pronounced. At closer and farther distances, the model's predictions align with the expected nonlinear relationship, confirming its robustness across different depth ranges. Optimal prediction accuracy is

notably achieved within the 50 cm to 250 cm range, illustrating the model's proficiency in navigating the complexities of human eye behavior.

### C. Performance Range

Analyzing individual subject performances offers valuable perspectives on the model's operational range. Subject 3 exemplifies the model's potential, with an impressive MAE under 5.9 cm, as depicted in the aligned actual and predicted values (Figure 6, left). This near-optimal alignment highlights FOVAL's ability to closely mimic natural eye movements. Conversely, Subject 25's performance, illustrating an MAE around 14.0 cm (Figure 6, right), underscores the challenges in achieving uniform accuracy across all subjects. This variance could stem from individual differences in eye physiology or disparities in eye-tracking data quality. It suggests a need for

## True vs. Predicted Values

### Comparing Strong and Weak Predictions



Fig. 6. Direct comparison of a strong and a weak prediction subject. **Left:** Subject 3, focal depth estimation with extremely low average MAE of 5.9 cm. Plotting true values versus predictions in ascending order shows the high alignment of the residuals with the optimal trend line. **Right:** Subject 25 focal depth estimation with a high average MAE of 14.0 cm. Plotting true values versus predictions reveals a challenging alignment process. The values are sorted for display purposes.

model refinement or improved tracking sensor approaches to enhance performance uniformly.

The residual plot for subject three predominantly features residuals along the optimal diagonal trend line, where each prediction matches the ground truth nearly perfectly, resulting in zero error. The few peaks suggest that either outliers are still present or these ranges are hard to predict. This pattern suggests a characteristic oscillation around the desired outcome, creating a wave-like pattern that oscillates around the diagonal line. Such a distribution indicates that FOVAL generally aligns well with the depth values. It occasionally strays from the optimal path, suggesting potential areas for model refinement. This oscillatory error pattern might hint at the necessity for additional epochs or adjustments in the model’s hyperparameters to ensure that the learning process more consistently converges to the global minimum of the loss function. An overly aggressive learning rate or inadequate epoch count could cause the model to overshoot its target or settle prematurely before adequately minimizing the loss. As seen in Figure 6, FOVAL, on average, tends to overestimate depth values more than underestimate them. The gray shaded area in Figure 6 represents the confidence interval of the model’s predictions, indicating the range within which we can expect the true values to lie with a certain level of confidence. This area helps to visualize the uncertainty and variability in the model’s predictions. When looking at the residuals of subject 25, this tendency is also visible as the initial large peaks are higher than the correct depth, while only half of the data predictions have smaller, lower peaks.

#### D. Learning interpretation

To gain deeper insights into our findings, we analyzed the activation maps of FOVAL layers, focusing on empirical observations of the model’s behavior during Training. Interpreting the learning behavior of deep learning models is challenging,

but these empirical findings offer valuable understanding. As anticipated by our architectural design, the activation maps generated during the model’s Training provide compelling evidence of its ability to learn abstract features hierarchically. Figure 7 displays the feature maps of the layers for one subject across ten samples. The activations of the input layer show how the samples are perceived when put into the trained model. High activation outputs are yellow, while low values are dark blue. Each column in this layer corresponds to one feature, resulting in 54 columns. To simplify visualization, the feature activations are averaged across the time dimension, meaning all the same features of one sequence are averaged. Features 6 through 8 exhibit consistent color coding, indicating minimal variance across samples. This consistency is due to these features representing the origin data of the eyes, which remains relatively constant and is only needed for calculating higher-order features. Their stability is attributed to their definition within the coordinate system of the glasses rather than in world coordinates. In the ELU layer, it is apparent that the model focuses on specific features of the sequence data with the highest activation. This layer involves more than 450 features, though only a subset exhibits significant activation values. This is typical due to the nature of activation functions like ELU, which set many activations to zero. Most samples display recognizable activation patterns, but there are notable exceptions. For instance, samples 5, 6, 8, and 9 show different activation patterns compared to the majority. These samples belong to higher depth values. Conversely, samples 0, 1, 2, and 4 show lower activations and correspond to smaller depth values. This variability suggests that our subject-invariant model can adapt to diverse input characteristics rather than relying on a single, uniform activation pattern across all subjects. We observed that different patterns emerge for various depth ranges, indicating that the model uses different combinations of features to predict different depths. This might correlate with the vergence-depth relationship, which is assumed to be

nonlinear for short and far ranges but linear in the mid-range. The model’s flexibility and robustness in adapting to these varying patterns highlight its ability to capture the complex relationships in the data accurately.

## V. DISCUSSION

This study introduced FOVAL, a calibration-free method for estimating focal depth using machine learning to analyze eye movement features in short sequences. Our approach achieved a mean absolute error (MAE) of less than 10 cm, surpassing traditional eye-tracking methods that require extensive calibration and setting a new standard in focal depth estimation accuracy. FOVAL’s superior performance compared to calibration-dependent methods underscores its robustness and practical applicability. The model’s lower MAE highlights its potential for real-world applications where frequent recalibration is impractical. The variability in performance among subjects suggests that while FOVAL generalizes well, individual differences in eye physiology and eye-tracking data quality need further consideration. The primary strength of this study lies in demonstrating a successful calibration-free approach to depth estimation using LSTM networks and domain-specific feature engineering. This innovation addresses a significant barrier to the practical use of autofocal glasses. Our methodology, particularly the detailed preprocessing pipeline and robust model architecture, offers a blueprint for future research aiming to eliminate calibration in similar applications.

## VI. LIMITATIONS

Despite its successes, the FOVAL model exhibits variability in performance among different subjects, highlighting an area for improvement. This variability underscores the challenge of achieving universal applicability while accommodating individual physiological differences. The primary tool for data capture, eye tracker cameras, may exhibit variable accuracy and precision across different individuals due to factors such as eye morphology. To mitigate these discrepancies, a meticulous evaluation process of eye-tracking performance for each subject is paramount. This would involve standardizing data collection protocols and implementing quality control measures to identify and correct potential anomalies in the data, ensuring consistent quality and reducing subject-specific biases. Additionally, our results were confirmed on only two datasets comprising 25 participants, using two different eye-tracking systems. For autofocals, it would be interesting to see how well the model performs in a large-scale real-world study involving an autofocal prototype.

## VII. IMPLICATIONS

FOVAL significantly enhances the usability of autofocal glasses by eliminating the need for user-specific calibration, making these devices more practical for daily use. Beyond autofocal glasses, FOVAL’s application in VR/AR environments can improve user immersion and interaction by accurately estimating focal depth in real-time. This has far-reaching implications for educational, medical, and entertainment applications. For instance, in medical fields such as

microscopy, arthroscopy, and robotic surgery, precise depth estimation can revolutionize how microscopic entities are visualized and analyzed, enhancing the clarity and depth of 3D imaging. FOVAL can also improve the user experience in VR by rendering environments with realistic spatial dynamics, and in AR, it allows for the seamless integration of digital objects into the real world. Future research should focus on refining the model to further reduce subject variability and enhance robustness so that the worst result for a subject is still under 10 cm MAE. This could involve more sophisticated data preprocessing techniques or improvements in eye-tracking technology. Attention layers might also reveal more robust predictions as the model can weigh features specifically for different subjects or patterns. Exploring transfer learning and few-shot learning could allow FOVAL to be adapted for related applications with minimal additional data, increasing its versatility. Investigating the integration of higher-quality eye-tracking systems and additional physiological data could further improve the model’s accuracy and generalizability. Developing methods to handle outliers and noise better could lead to more consistent performance across a broader range of subjects. Visualization of activations could help understand feature contribution to predictions or cluster subjects into subgroups, providing deeper insights into the model’s behavior and human gaze patterns.

## VIII. DATA AVAILABILITY STATEMENT

To ensure the reproducibility of our results, we have made all data and code publicly available at the Open Science Framework (OSF) repository: [https://t.ly/g\\_5ta](https://t.ly/g_5ta)

## ACKNOWLEDGMENTS

This work was supported by the German Research Foundation (DFG): SFB 1233, Robust Vision: Inference Principles and Neural Mechanisms, TP T01, project number: 276693517. We acknowledge support from the Open Access Publication Fund of the University of Tübingen.

## REFERENCES

- [1] Rajat Agarwala, Olga Lukashova Sanz, Immanuel P Seitz, Felix F Reichel, and Siegfried Wahl. Evaluation of a liquid membrane-based tunable lens and a solid-state lidar camera feedback system for presbyopia. *Biomedical Optics Express*, 13(11):5849–5859, 2022.
- [2] Takuya Akiba, Shotaro Sano, Toshihiko Yanase, Takeru Ohta, and Masanori Koyama. Optuna: A next-generation hyperparameter optimization framework. In *Proceedings of the 25th ACM SIGKDD international conference on knowledge discovery & data mining*, pages 2623–2631, 2019.
- [3] David A Atchison. Accommodation and presbyopia. *Ophthalmic and Physiological Optics*, 15(4):255–272, 1995.
- [4] S. Babilon, Paul Myland, L. Schlestein, Julian Klabes, and T. Khanh. High-resolution depth measurements in digital microscopic surgery. *Engineering Reports*, 3, 2020.

- [5] Nguyen Binh-Khiem, Kiyoshi Matsumoto, and Isao Shimoyama. Polymer thin film deposited on liquid for varifocal encapsulated liquid lenses. *Applied physics letters*, 93(12), 2008.
- [6] Christopher M. Bishop. *Pattern Recognition and Machine Learning*. Springer, 2006.
- [7] George EP Box and David R Cox. An analysis of transformations. *Journal of the Royal Statistical Society: Series B (Methodological)*, 26(2):211–243, 1964.
- [8] W Neil Charman. The eye in focus: accommodation and presbyopia. *Clinical and experimental optometry*, 91(3):207–225, 2008.
- [9] W Neil Charman. Developments in the correction of presbyopia i: spectacle and contact lenses. *Ophthalmic and Physiological Optics*, 34(1):8–29, 2014.
- [10] Cheng-Yang Fu, Mykhailo Shvets, and Alexander C Berg. Retinamask: Learning to predict masks improves state-of-the-art single-shot detection for free. *arXiv preprint arXiv:1901.03353*, 2019.
- [11] Ian Goodfellow, Yoshua Bengio, and Aaron Courville. *Deep Learning*. MIT Press, 2016.
- [12] Trevor Hastie, Robert Tibshirani, and Jerome Friedman. *The Elements of Statistical Learning: Data Mining, Inference, and Prediction*. Springer, 2009.
- [13] David C Hoaglin, Frederick Mosteller, and John W Tukey. *Understanding robust and exploratory data analysis*, volume 76. John Wiley & Sons, 2000.
- [14] Sepp Hochreiter and Jürgen Schmidhuber. Long short-term memory. *Neural computation*, 9(8):1735–1780, 1997.
- [15] Benedikt W Hosp, Yannick Sauer, Björn Severitt, Rajat Agarwala, and Siegfried Wahl. Simulation of various tuning methods in autofocals using a virtual reality headset. *Optics Continuum*, 3(8):1273–1290, 2024.
- [16] Benedikt W Hosp, Florian Schultz, Oliver Höner, and Enkelejda Kasneci. Soccer goalkeeper expertise identification based on eye movements. *PloS one*, 16(5):e0251070, 2021.
- [17] Baoru Huang, Jian-Qing Zheng, Anh Nguyen, Chi Xu, I. Gkouzionis, K. Vyas, D. Tuch, S. Giannarou, and D. Elson. Self-supervised depth estimation in laparoscopic image using 3d geometric consistency. *ArXiv*, abs/2208.08407, 2022.
- [18] Sergey Ioffe and Christian Szegedy. Batch normalization: Accelerating deep network training by reducing internal covariate shift. In *International conference on machine learning*, pages 448–456. pmlr, 2015.
- [19] Louise Johnson, John G Buckley, Andy J Scally, and David B Elliott. Multifocal spectacles increase variability in toe clearance and risk of tripping in the elderly. *Investigative Ophthalmology & Visual Science*, 48(4):1466–1471, 2007.
- [20] Richard Arnold Johnson and Dean W Wichern. *Applied Multivariate Statistical Analysis*. Pearson Education, 2012.
- [21] Mohit U Karkhanis, Chayanjit Ghosh, Aishwaryadev Banerjee, Nazmul Hasan, Rugved Likhite, Tridib Ghosh, Hanseup Kim, and Carlos H Mastrangelo. Correcting presbyopia with autofocusing liquid-lens eyeglasses. *IEEE Transactions on Biomedical Engineering*, 69(1):390–400, 2021.
- [22] Minseok Kim, S. Choi, Kyeong-Beom Park, and Jae Yeol Lee. A hybrid approach to industrial augmented reality using deep learning-based facility segmentation and depth prediction. *Sensors (Basel, Switzerland)*, 21, 2021.
- [23] Diederik P Kingma and Jimmy Ba. Adam: A method for stochastic optimization. *arXiv preprint arXiv:1412.6980*, 2014.
- [24] Brooke Krajancich, Petr Kellnhofer, and Gordon Wetzstein. Optimizing depth perception in virtual and augmented reality through gaze-contingent stereo rendering. *ACM Transactions on Graphics (TOG)*, 39:1–10, 2020.
- [25] Yann LeCun, Yoshua Bengio, and Geoffrey Hinton. Deep learning. *Nature*, 521(7553):436–444, 2015.
- [26] Yann LeCun, Léon Bottou, Yoshua Bengio, and Patrick Haffner. Gradient-based learning applied to document recognition. *Proceedings of the IEEE*, 86(11):2278–2324, 1998.
- [27] Guoqiang Li, David L Mathine, Pouria Valley, Pekka Äyräs, Joshua N Haddock, MS Giridhar, Gregory Williby, Jim Schwiegerling, Gerald R Meredith, Bernard Kippelen, et al. Switchable electro-optic diffractive lens with high efficiency for ophthalmic applications. *Proceedings of the National Academy of Sciences*, 103(16):6100–6104, 2006.
- [28] Ling Li, Xiaojian Li, Shanlin Yang, Shuai Ding, A. Jolfaei, and Xi Zheng. Unsupervised-learning-based continuous depth and motion estimation with monocular endoscopy for virtual reality minimally invasive surgery. *IEEE Transactions on Industrial Informatics*, 17:3920–3928, 2020.
- [29] Weizhi Li, Weirong Mo, Xu Zhang, J. Squiers, Yang Lu, E. Sellke, Wensheng Fan, J. Dimaio, and Jeffrey E. Thatcher. Outlier detection and removal improves accuracy of machine learning approach to multispectral burn diagnostic imaging. *Journal of Biomedical Optics*, 20, 2015.
- [30] Xingtong Liu, Ayushi Sinha, M. Ishii, Gregory Hager, A. Reiter, R. Taylor, and M. Unberath. Dense depth estimation in monocular endoscopy with self-supervised learning methods. *IEEE Transactions on Medical Imaging*, 39:1438–1447, 2019.
- [31] Stephen R Lord, Julia Dayhew, and Amelia Howland. Multifocal glasses impair edge-contrast sensitivity and depth perception and increase the risk of falls in older people. *Journal of the American Geriatrics Society*, 50(11):1760–1766, 2002.
- [32] Ilya Loshchilov and Frank Hutter. Decoupled weight decay regularization. *arXiv preprint arXiv:1711.05101*, 2017.
- [33] M. Maniruzzaman, M. Rahman, Md. Al-Mehedi Hasan, Harman S. Suri, M. Abedin, A. El-Baz, and J. Suri. Accurate diabetes risk stratification using machine learning: Role of missing value and outliers. *Journal of Medical Systems*, 42, 2018.
- [34] Armin Masoumian, Hatem A. Rashwan, Julián Cristiano,

- M. Salman Asif, and D. Puig. Monocular depth estimation using deep learning: A review. *Sensors (Basel, Switzerland)*, 22, 2022.
- [35] Esteban Gutierrez Mlot, H. Bahmani, S. Wahl, and Enkelejda Kasneci. 3d gaze estimation using eye vergence. pages 125–131, 2016.
- [36] M. Nyström and K. Holmqvist. An adaptive algorithm for fixation, saccade, and glissade detection in eyetracking data. *Behavior Research Methods*, 42:188–204, 2010.
- [37] Jason W Osborne. Improving your data transformations: Applying the box-cox transformation. *Practical Assessment, Research, and Evaluation*, 15(1):12, 2010.
- [38] Nitish Padmanaban, Robert Konrad, and Gordon Wetzstein. Autofocals: gaze-contingent eyeglasses for presbyopes. In *ACM SIGGRAPH 2018 Emerging Technologies*, pages 1–2. 2018.
- [39] Nitish Padmanaban, Robert Konrad, and Gordon Wetzstein. Autofocals: Evaluating gaze-contingent eyeglasses for presbyopes. *Science Advances*, 5(6):eaav6187, 2019.
- [40] Nitish Padmanaban, Robert K. Konrad, and Gordon Wetzstein. Autofocals: evaluating gaze-contingent eyeglasses for presbyopes. In *ACM SIGGRAPH 2019 Talks*, SIGGRAPH ’19, New York, NY, USA, 2019. Association for Computing Machinery.
- [41] F. Pedregosa, G. Varoquaux, A. Gramfort, V. Michel, B. Thirion, O. Grisel, M. Blondel, P. Prettenhofer, R. Weiss, V. Dubourg, J. Vanderplas, A. Passos, D. Cournapeau, M. Brucher, M. Perrot, and E. Duchesnay. Scikit-learn: Machine Learning in Python. <https://scikit-learn.org>, 2011.
- [42] H. Perez and J. Tah. Improving the accuracy of convolutional neural networks by identifying and removing outlier images in datasets using t-sne. *Mathematics*, 2020.
- [43] David R Pope. Progressive addition lenses: history, design, wearer satisfaction and trends. In *Vision science and its applications*, page NW9. Optica Publishing Group, 2000.
- [44] Laksmi Rahadiani, Fumihiko Sakaue, and J. Sato. Depth estimation from single hazy images with 2-phase training. *2020 International Conference on Advanced Computer Science and Information Systems (ICACSIS)*, pages 309–316, 2020.
- [45] Shaoqing Ren, Kaiming He, Ross Girshick, and Jian Sun. Faster r-cnn: Towards real-time object detection with region proposal networks. *IEEE transactions on pattern analysis and machine intelligence*, 39(6):1137–1149, 2016.
- [46] Jelle De Smet. Morrow Eyeware: An Introduction to Morrow’s Autofocal Tunable Lens Technology. In Conference Chair, editor, *SPIE AVR21 Industry Talks II*, volume 11764, page 117640K. International Society for Optics and Photonics, SPIE, 2021.
- [47] Nitish Srivastava, Geoffrey Hinton, Alex Krizhevsky, Ilya Sutskever, and Ruslan Salakhutdinov. Dropout: a simple way to prevent neural networks from overfitting. *The journal of machine learning research*, 15(1):1929–1958, 2014.
- [48] Abigail Stone, Srijith Rajeev, S. P. Rao, K. Panetta, S. Agaian, Aaron Gardony, Jessica Nordlund, and Rebecca Skantar. Gaze depth estimation for eye-tracking systems. 12526:125260N–125260N–10, 2023.
- [49] Jun’Nosuke Takarabe, Irawati Nurmala Sari, and Weiwei Du. Depth map estimation of single-view image using smartphone camera for a 3-dimension image generation in augmented reality. *2023 Sixth International Symposium on Computer, Consumer and Control (IS3C)*, pages 167–170, 2023.
- [50] Takafumi Taketomi, Tomokazu Sato, and N. Yokoya. Real-time and accurate extrinsic camera parameter estimation using feature landmark database for augmented reality. *Comput. Graph.*, 35:768–777, 2011.
- [51] M. Tistarelli and G. Sandini. Estimation of depth from motion using an anthropomorphic visual sensor. *Image Vis. Comput.*, 8:271–278, 1990.
- [52] Atiq ur Rehman and S. Belhaouari. Unsupervised outlier detection in multidimensional data. *Journal of Big Data*, 8, 2021.
- [53] HP Vinutha, B Poornima, and BM Sagar. Detection of outliers using interquartile range technique from intrusion dataset. In *Information and decision sciences: Proceedings of the 6th international conference on ficta*, pages 511–518. Springer, 2018.
- [54] VRgineers. Xtal vr headset. VRgineers, Inc., 2024. Accessed: 2024-03-22.
- [55] Lihui Wang, Alvaro Cassinelli, Hiromasa Oku, and Masatoshi Ishikawa. A pair of diopter-adjustable eyeglasses for presbyopia correction. In *Novel Optical Systems Design and Optimization XVII*, volume 9193, pages 369–378. SPIE, 2014.
- [56] Changxu Zhu. For higher accuracy: 3d eye movement gaze depth estimation method based on mix-tn. In *Journal of Physics: Conference Series*, volume 2646, page 012044. IOP Publishing, 2023.

## IX. APPENDIX

### A. Feature computation equations

This section describes our specific computations for each feature in the feature engineering process.

*Interpupillary Distance (IPD)*: The IPD is calculated as the Euclidean distance between the gaze origins of the right and left eyes:

$$IPD = \sqrt{(\Delta X)^2 + (\Delta Y)^2 + (\Delta Z)^2} \quad (16)$$

where  $\Delta X$ ,  $\Delta Y$ , and  $\Delta Z$  are the differences in the  $X$ ,  $Y$ , and  $Z$  coordinates of the right and left eye gaze origins, respectively.

#### Vergence Angle

The vergence angle (VA) between the gaze directions of the right and left eyes is calculated using the dot product, normalized by the magnitudes of the gaze direction vectors:

$$VA = \arccos \left( \frac{\vec{R} \cdot \vec{L}}{\|\vec{R}\| \|\vec{L}\|} \right) \quad (17)$$

where  $\vec{R}$  and  $\vec{L}$  are the gaze direction vectors for the right and left eyes, respectively.

#### Normalized Vergence Angle

Normalizing the vergence angle between -1 and 1 provides a standardized scale for this feature, making the model's learning process less sensitive to the absolute scale of the original angles. It's calculated as:

$$VA_{\text{normalized}} = 2 \left( \frac{VA - \min(VA)}{\max(VA) - \min(VA)} \right) - 1 \quad (18)$$

#### Vergence Depth Calculation

Vergence Depth (VD) is computed based on the vergence angle and the IPD, assuming a simple geometric model of eye vergence:

$$VD = \frac{IPD}{2 \tan \left( \frac{VA}{2} \right)} \quad (19)$$

This depth is then converted from meters to centimeters. Please note that specific calculations such as velocity, acceleration, and angular differences require sequential data points and depend on the temporal resolution of the data collected.

#### Normalized Depth

The normalized depth for each observation is calculated as:

$$VD_{\text{normalized}} = \frac{VD - \min(VD)}{\max(VD) - \min(VD)} \quad (20)$$

#### Directional Magnitude

The magnitude of gaze direction vectors for the right and left eyes are computed using the Euclidean norm:

$$\vec{D}_R = \|\vec{R}\| \quad (21)$$

$$\vec{D}_L = \|\vec{L}\| \quad (22)$$

where  $\vec{R}$  and  $\vec{L}$  are the gaze direction vectors for the right and left eyes, respectively.

### Gaze Direction Cosine Angles

The cosine of vergence angles, derived from the eye vergence angle data, represents the orientation difference between the gaze directions of the two eyes. This feature is essential because it captures the degree of alignment or disparity between the eyes' focus, which can indicate depth perception and the point of focus in 3D space. The cosine of the vergence angle is calculated as:

$$\text{Cosine Angles} = \cos(VA) \quad (23)$$

### Gaze Point Distance

This feature calculates the Euclidean distance between the directions of the right and left eyes using their  $X$  and  $Y$  components. This distance can indicate how convergent or divergent the gaze is, which, like the vergence angle, relates to depth perception and focus. The Euclidean distance between the gaze points of the right and left eyes is computed as:

$$POR_{\text{Distance}} = \sqrt{(\vec{R}_X - \vec{R}_Y)^2 + (\vec{R}_Y - \vec{R}_X)^2} \quad (24)$$

where  $\vec{R}_X$  represents the gaze direction of the right eye in the  $x$  direction.

### Angular Difference between Gaze Directions

The angular difference between the gaze directions is calculated using the dot product and magnitude of gaze direction vectors:

$$\vec{D}_{\text{Angle}} = \arccos \left( \frac{\vec{D}_R \cdot \vec{D}_L}{\|\vec{D}_R\| \|\vec{D}_L\|} \right) \quad (25)$$

### Velocity and Acceleration

Velocity and acceleration are derived from the gaze direction  $X$ -component (similar computations apply for  $Y$  and  $Z$  components) and the left eye:

$$\text{Velocity}_X = \Delta \vec{R}_X \quad (26)$$

$$\text{Acceleration}_X = \Delta \text{Velocity}_X \quad (27)$$

### Gaze Direction Ratios ( $\vec{R}_{X,Y,Z}$ )

$$R_X = \frac{\vec{R}}{L_X} \quad (28)$$

$$R_Y = \frac{\vec{R}}{L_Y} \quad (29)$$

$$R_Z = \frac{\vec{R}}{L_Z} \quad (30)$$

### Ratio of Delta Gaze ( $R_{\Delta \text{Gaze}_{XY}}$ )

$$R_{\Delta \text{Gaze}_{XY}} = \frac{R_{\Delta \text{Gaze}_X}}{R_{\Delta \text{Gaze}_Y}} \quad (31)$$

### Gaze Direction Angle

The angle between the gaze direction vectors of the right and left eyes:

$$\vec{D}_{\text{Angle}} = \arccos \left( \frac{\vec{R} \cdot \vec{L}}{\|\vec{R}\| \|\vec{L}\|} \right) \quad (32)$$

### Relative Change in Vergence Angle

The change in vergence angle over time (or between sequential observations):

$$\text{Relative Change VA} = V_t - V_{t-1} \quad (33)$$

### Ratio of Directional Magnitudes

The ratio of the directional magnitudes (norms of gaze direction vectors) for the right and left eyes:

$$\text{Ratio}_{\vec{D}} = \frac{\|\vec{D}_R\|}{\|\vec{D}_L\|} \quad (34)$$

### Gaze Point Depth Difference

The difference in depth (Z-coordinate) between the right and left gaze points:

$$\Delta \text{Gaze Point}_{\text{Depth}} = R_Z - L_Z \quad (35)$$

### Ratios of World Gaze Direction Components

The ratios of corresponding components of the world gaze direction vectors for the right and left eyes:

$$\text{Ratio } \vec{D}_{\text{World},X} = \frac{R_X}{L_X} \quad (36)$$

$$\text{Ratio } \vec{D}_{\text{World},Y} = \frac{R_Y}{L_Y} \quad (37)$$

$$\text{Ratio } \vec{D}_{\text{World},Z} = \frac{R_Z}{L_Z} \quad (38)$$

### Velocity and Acceleration

The rate of change (velocity) and the rate of change of the rate of change (acceleration) in a given component (e.g., X) of the gaze direction:

$$\text{Velocity}_X = X_t - X_{t-1} \quad (39)$$

$$\text{Acceleration}_X = \text{Velocity}_{X_t} - \text{Velocity}_{X_{t-1}} \quad (40)$$

### Angular Difference X

The difference in the X-component (horizontal) of the angular gaze direction between the right and left eyes:

$$\text{Angular Difference}_X = \theta_{RX} - \theta_{LX} \quad (41)$$

## Feature Map

Neural activations of layers

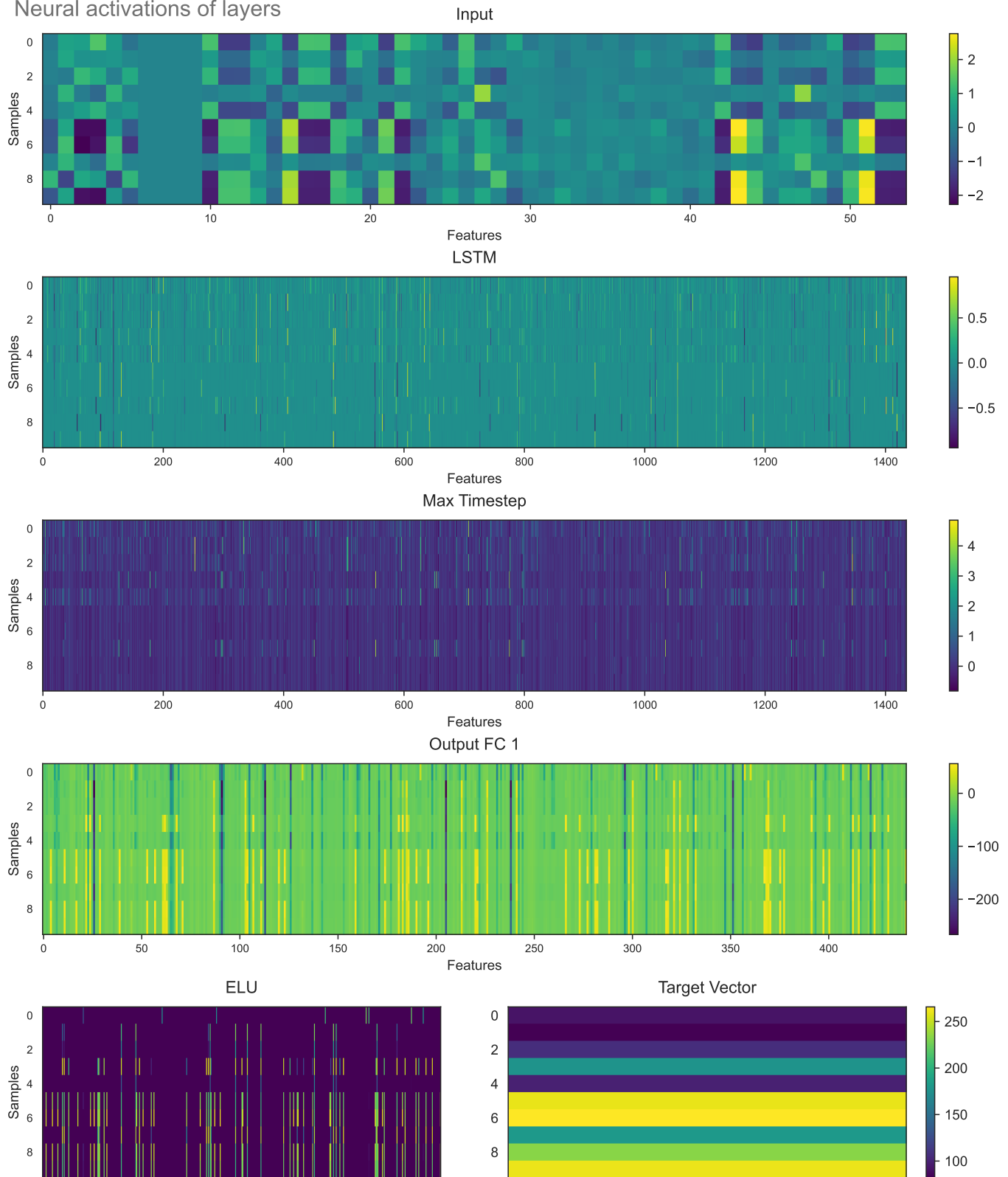


Fig. 7. Layers of the model showing the evolution of activations and expansion of features across layers. The Y-axis exemplifies ten samples (0-9), while the X-axis corresponds to features. Most important for model interpretation is the relationship between the input to the ELU layer and the resulting output vector of the model. As in the ELU layer, several patterns are visible; not one single pattern can describe the output alone, suggesting clustering is happening to estimate depth differently for different samples.